

A2: Mass and Density Profiles of White Dwarfs

Deriving the mass-radius and density-radius relations from the Equation of State

T. Harvey¹

Physics and Astronomy, University of Southampton, Southampton
e-mail: th4g18@soton.ac.uk

October 29, 2021

ABSTRACT

Aims. In this paper the mass-radius relation for white dwarfs has been computed for both carbon/oxygen and iron core white dwarfs, and the corresponding Chandrasekhar masses have been determined. The aim was to produce a simple model which accurately matched observations of white dwarf masses and radii.

Methods. The white dwarf has been modelled as a degenerate near-relativistic Fermi electron gas, and the equation of state describing such a system has been derived. The differential equations describing the mass and density distributions have been derived and solved using a Runge-Kutta 4(5) ODE solver from SciPy. The central density of the white dwarf was varied to model white dwarfs of varying total masses, which were used to produce the overall mass-radius relation for carbon and iron white dwarfs.

Results. The Chandrasekhar mass (upper mass limit) for both carbon-oxygen and iron white dwarfs were calculated from the mass-radius relations to be $(1.44 \pm 0.002)M_{\odot}$ and $(1.24 \pm 0.001)M_{\odot}$ respectively. The mass-radius relations were compared to online catalogs of known white dwarf masses and radii, and were within error of the theoretical curves, especially for higher mass white dwarfs. There was some discrepancy between the predicted and observational data for lower mass white dwarfs which was attributed to the simplicity of the model not accounting for deviations from degeneracy at high radii, and the lack of modelling of the outer hydrogen/helium envelopes that are observed in white dwarfs.

1. Introduction

The first white dwarf discovered was 40 Eridani B by William Herschel in 1783 but it took until 1910 to be identified as a new class of star that despite having a very small absolute magnitude, appeared white in colour (Herschel 1785). This went against the general observation that most low luminosity stars appear red because of Wien's displacement law. Since then many thousands of white dwarfs have been discovered, with notable catalogs including those derived from the Sloan Digital Sky Survey (Eisenstein et al. 2006, Kleinman et al. 2013), Hipparcos (Provencal et al. 1998) and more recently from Gaia (Xu et al. 2020, Tremblay et al. 2017). For example the SDSS DR7 white dwarf catalog contains 19,712 white dwarfs. In Gentile Fusillo et al. 2018 the recent Gaia DR2 was used to build a catalog of 260,000 high confidence white dwarf candidates. These large data sets let us compare theoretical models of white dwarfs to observations, letting us constrain properties of white dwarfs such as the mass-radius relation.

The nearest white dwarf, Sirius B, shown in Figure 1, is the binary companion of the brightest star in the night sky, Sirius A, which is A0/A1 class main-sequence star. Sirius B was the 2nd white dwarf to be discovered, and is one of the 3 "classic" white dwarfs discovered to be white dwarfs in the early 20th century. The others are 40 Eridani B and Procyon B. Observations of Sirius B have been hampered by its proximity to its bright companion, but the binary system has allowed accurate determination of the orbital parameters.

In this paper a white dwarf will be modelled by treating it as a degenerate electron gas constrained by the differential equilibrium equations of a star with spherical symmetry. These equations will be solved by a numerical (Runge-Kutta) method in order to constrain the density-radius and mass-radius relations of

white dwarfs. The observed mass-radius relations of these "classical" white dwarfs, and more recent observations mentioned above, will be used to evaluate the accuracy of the model.

2. Theory

2.1. Basics of White Dwarfs

White dwarfs belong to a category of astronomical bodies called compact objects, along with neutron stars and black holes. This class of object are characterised by several key parameters.

1. They represent the end point of a stellar lifecycle.
2. They do not burn nuclear fuel, and don't balance gravity by thermal pressure.
3. They have a very compact size - white dwarfs are normally between 0.8% and 2% the radius of the Sun (Shipman 1979).

White dwarfs are formed from main sequence stars that have come to the end of their lives. They form from stars similar in mass to the Sun, which when it has burnt through its hydrogen core will start burning helium into carbon and oxygen via the triple- α process (Oberhummer et al. 2000). This is known as the red giant stage, as the outer layers of the star expand and cool. The carbon and oxygen build up in the core as the helium burning continues. When the helium is exhausted the star will begin to fuse carbon and oxygen if it is massive enough. If it cannot produce the required temperatures and pressures (around 5×10^8 K for carbon-12 burning from Pols 2011), then fusion can no longer occur.

The outer envelope is expelled, forming a diffuse cloud of gas called a planetary nebula. The inert core collapses forming a white dwarf. This will occur for stars between $0.5 M_{\odot}$ and $8 M_{\odot}$,

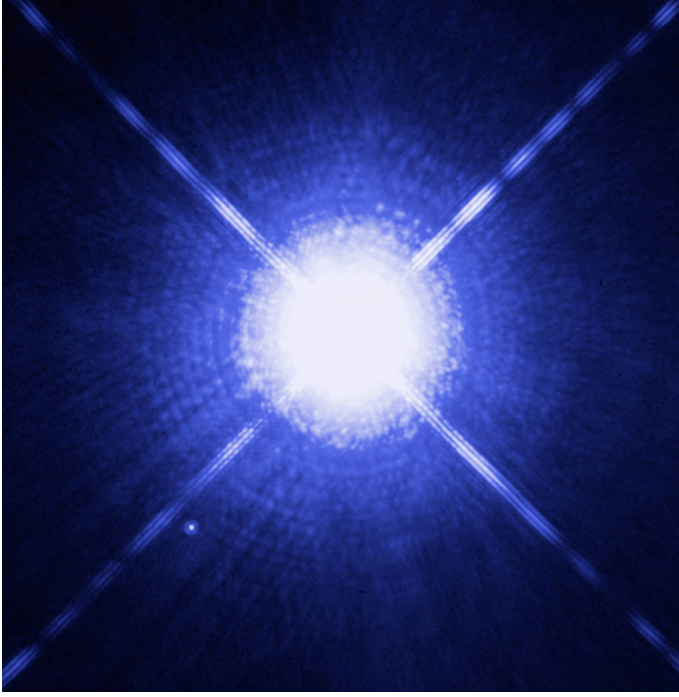


Fig. 1. Image showing Sirius A and B. Sirius B is the small dot in the bottom left. Sirius B is the nearest white dwarf to Earth, at 8.6 light years away. Image Credit: NASA, ESA, H. Bond (STScI) and M. Barstow (University of Leicester)

leaving behind a Carbon-Oxygen (CO) white dwarf (Camenzind 2007). These are the most common type of white dwarf. Lower mass stars are thought to be able to form Helium white dwarfs (Liebert et al. 2004), as they lack the mass to reach the temperature for helium fusion. Mass loss in binary systems is thought to be the cause of observed helium white dwarfs, as otherwise the low mass main sequence progenitor is expected to be stable for a time greater than the current age of the universe (Benvenuto & De Vito 2005, Sarna et al. 2001). Stars with mass around $8 M_{\odot}$ to $10 M_{\odot}$ which just lack the required mass to form a neutron star or black hole, can form white dwarfs made of oxygen, neon and magnesium (Nomoto 1984, Woosley et al. 2002).

The more exotic white dwarfs still have outer layers of helium and a hydrogen envelope, and so are hard to differentiate as they produce the same spectra Guo et al. 2021. There has also been speculation on the existence of iron-core white dwarfs (Isern et al. 1991, Catalán et al. 2007) due to early Hipparcos data (Provencal et al. 1998), and while there are some observations that support their existence, Fe core white dwarfs would have to form from very specific progenitors in order to avoid the fate of a core-collapse supernovae that befalls the vast majority of iron core stars (Catalán et al. 2007).

These white dwarfs are very unusual objects, with radii of around that of Earth ($0.09R_{\odot}$), containing greater than the mass of the Sun. This suggests a white dwarf has an average density of greater than $10^6 g cm^{-3}$ (Camenzind 2007). This is incredibly dense, and the inward force of gravity is balanced by electron degeneracy pressure - the repulsion between electrons stops the star from collapsing completely. This is due to the Pauli exclusion principle, which states that no two electrons can occupy the same state and that they must obey Fermi-Dirac statistics since they are fermions. In a white dwarf the densities are so high that electrons must occupy very high energy states, since the lower energy states are full. Increasing the electron density in a volume

would cause higher energy states to be occupied, increasing the kinetic energy of the electrons and hence increasing the pressure between them. This is known as electron degeneracy (Fowler 1926). This pressure depends only on the density of the material, not the temperature. This result means that the radius of a white dwarf is inversely proportional to the mass - more massive white dwarfs have a smaller radius. In a white dwarf the atoms are at such high densities that the electrons are considered relativistic and must be modelled as a relativistic degenerate Fermi gas. The cutoff between non-relativistic and relativistic electrons is traditionally given as $\rho = 10^6 g cm^{-3}$.

There is a limit to the support electron degeneracy pressure can provide, known as the Chandrasekhar limit. It was famously derived in 1931 in Chandrasekhar 1931 as

$$M_{ch} = \frac{5.76M_{\odot}}{\mu_e^2} \quad (1)$$

where μ_e is the average molecular weight per electron of the star. For carbon-oxygen white dwarfs, μ_e is 2, giving an upper-mass limit of $1.44M_{\odot}$. For an Fe white dwarf, the limit is $1.24M_{\odot}$. For a white dwarf that exceeded this limit if no nuclear reactions occurred would collapse into a neutron star, another type of compact object balanced by neutron degeneracy pressure. White dwarfs in binary systems often accrete mass onto their surfaces (Mohamed & Podsiadlowski 2007) from the companion, which can lead to the white dwarf being destroyed in a Type Ia supernovae as it approaches the Chandrasekhar mass (Hillebrandt & Niemeyer 2000). The lowest observed white dwarf has a mass of $0.17M_{\odot}$, and most C-O white dwarfs have masses between $0.5M_{\odot}$ and $0.7M_{\odot}$ (Kepler et al. 2007).

As white dwarfs do not produce energy, they slowly cool and fade as they radiate away their stored energy. Thus older white dwarfs are dimmer than young white dwarfs. The interior structure of a white dwarf is thought to consist of an outer thin hydrogen envelope, a crust of non-degenerate matter and an interior of degenerate matter (Camenzind 2007). They are thought to have an onion-skin interior, with layers of increasingly heavy elements closer to the core. Since the equation of state does not depend on temperature, this interior is thought to have a roughly uniform temperature of around $10^7 K$ (Marshak 1940). White dwarfs have high effective surface temperatures, between 8000K and 40,000K (McCook & Sion 1999). One of the coolest white dwarfs known is WD 0346+246 (Hambly et al. 1997), at 3900K. Cooler white dwarfs will be more numerous because white dwarfs spend most of their lives at cooler temperatures. There are however very few white dwarfs below 4000K as they have not had time to cool further given the current age of the universe. As they radiate with $L \propto T^4$, as they reach lower temperatures they radiate more slowly and thus lose energy more slowly, so they cool slower.

2.2. Equations of State

The white dwarf will be modelled as a non-rotating uniform sphere of fluid in equilibrium, characterised by an equation of state specific to the properties of the fluid. For a rotating white dwarf the outward centrifugal force would provide a counter to gravity and have to be included in any analysis. Firstly the standard equation for hydrostatic equilibrium within a sphere is used, which relates the radial pressure gradient to the density $\rho(r)$ and mass $m(r)$ inside a shell of radius r . The complete derivation can be found within Pols 2011.

$$\frac{dP}{dr} = -\frac{Gm(r)\rho(r)}{r^2} \quad (2)$$

Next it is possible to manipulate the properties of differential equations to find the relation between the density gradient and pressure gradient.

$$\frac{dP}{dr} = \frac{d\rho}{dr} \frac{dP}{d\rho} \quad (3)$$

This lets us reframe Equation 2 as a function of density.

$$\frac{d\rho}{dr} = - \left(\frac{dP}{d\rho} \right)^{-1} \frac{Gm}{r^2} \rho \quad (4)$$

Another differential equation for the enclosed mass within a shell of the star at radius r and density ρ can also be defined. This is the 2nd differential equation to be solved.

$$\frac{dm}{dr} = 4\pi r^2 \rho \quad (5)$$

The next step is to find the Equation of State relating density and pressure to proceed further. A white dwarf is modelled as a fluid consisting of a single type of nuclei (e.g carbon or oxygen) along with their electrons. Homogeneity of the fluid has been assumed - in reality white dwarfs have distinct layers dominated by a particular type of nuclei e.g helium or carbon. Since the nuclei are much heavier than the electrons, they contribute almost nothing to the pressure of the gas since they move much more slowly at a given energy. The atoms would be completely ionised as the temperatures and densities are very high, so the electrons are free to move (Pols 2011). The simplifying assumption that all of the pressure comes from the electrons can be therefore be used. The fluid can be modelled as a degenerate Fermi electron gas.

Firstly very generally the pressure P of an ideal gas is given by the integral

$$P = \frac{1}{3} \int_0^\infty p v_p n(p) dp \quad (6)$$

where p is particle momentum, v_p is particle velocity, and $n(p)$ is number density of particles. Taken from Pols 2011. There are 3 cases for the velocity of the electrons:

1. Non-relativistic with $v_p = p/m$ and $\epsilon = p^2/2m$
2. Near relativistic with $v_p = p/\gamma m$ and $\epsilon = \sqrt{p^2 c^2 + m^2 c^4}$
3. Extremely relativistic with $v = c$ and $\epsilon = pc$

ϵ is the energy of the particle, c is the speed of light, m is the mass of the particle, p is the momentum of the particle and γ is the relativistic gamma factor:

$$\gamma = \frac{1}{\sqrt{1 - \left(\frac{v}{c}\right)^2}} \quad (7)$$

With some manipulation an expression for the velocity of the particle in the near-relativistic case is found as

$$v = \sqrt{\frac{(p/m)^2}{1 + \frac{(p/m)^2}{c^2}}} \quad (8)$$

Next the number density as a function of momentum for the degenerate electron gas is needed, assuming it is in local thermodynamic equilibrium. As fermions, electrons obey the Pauli exclusion principle and have an occupation fraction given by the Fermi-Dirac distribution (Dirac 1926):

$$f_{FD}(\epsilon) = \frac{1}{e^{(\epsilon_p - \mu)/kT} + 1} \quad (9)$$

which gives the fraction of quantum states of energy ϵ occupied at a temperature T . μ is the chemical potential and can be thought of as a normalisation constant determined by the total particle number.

The famous Heisenberg uncertainty principle (Heisenberg 1927), states that there is a limit to how well it is possible to simultaneously determine a particles position and momentum. In 3D, this is given as:

$$\Delta V \Delta^3 p \geq h^3 \quad (10)$$

For a particle constrained to a volume ΔV it occupies a volume h^3 in phase-space. For the volume the number of available quantum states for particles with momenta between p and $p + dp$ is therefore:

$$g(p)dp = g_s \frac{V}{h^3} 4\pi p^2 dp \quad (11)$$

The maximum number density of states for electrons with momentum p (electrons have $g_e = 2$ spin states) is:

$$g(p)dp/V = n_{\max}(p)dp = \frac{g_e}{h^3} 4\pi p^2 dp \quad (12)$$

The maximum number density of electrons is given by the product of $n_{\max}(p)dp$ and f_{FD} . For the electron gas inside the white dwarf to be completely degenerate, kT must be much less than the energy of the electron ϵ . White dwarfs are so dense that the electrons have momenta $p \geq m_e c$. This momenta corresponds to relativistic electrons (as assumed) so that $\epsilon \geq m_e c^2 \approx 5 \times 10^5 \text{ eV}$. This corresponds to a temperature of $T \ll m_e c^2/k \approx 6 \times 10^9 \text{ K}$. While the star is below this temperature the approximation of the electron gas as degenerate is good. As mentioned above, white dwarfs are thought to have a reasonably uniform temperature of 10^7 K throughout much of their interior, meaning that this approximation is suitable.

The way electrons are forced to occupy the lowest states also happens in other situations because of extremely low energy, i.e at low temperature, which is why the electron gas can be modelled as having a temperature of 0. However in this case it occurs because of the extremely high densities forcing the electrons into higher states than they would otherwise occupy. This means they have higher energy and momentum and exert a higher pressure - this is the electron degeneracy pressure.

Because the electrons are completely degenerate, the momentum distribution can be modelled as a step function, with a maximum at p_F before dropping to 0. This is shown in Figure 2, which shows the momentum distribution calculated from the above equations for 2 different densities, showing that all the momentum states are occupied up to the Fermi momentum, and none beyond it. This means that the momentum number density is more simply:

$$n_e(p) = \begin{cases} \frac{8\pi p^2}{h^3} & p < p_F \\ 0 & p > p_F \end{cases} \quad (13)$$

This maximum value is called the Fermi momentum p_F and it is determined from the constraint

$$n_e = \int_0^{p_F} n_e(p) dp \quad (14)$$

The density ρ is related to the electron number density n_e with the mass of a nucleon m_p (neglecting mass difference between protons and neutrons), and the average number of electrons per

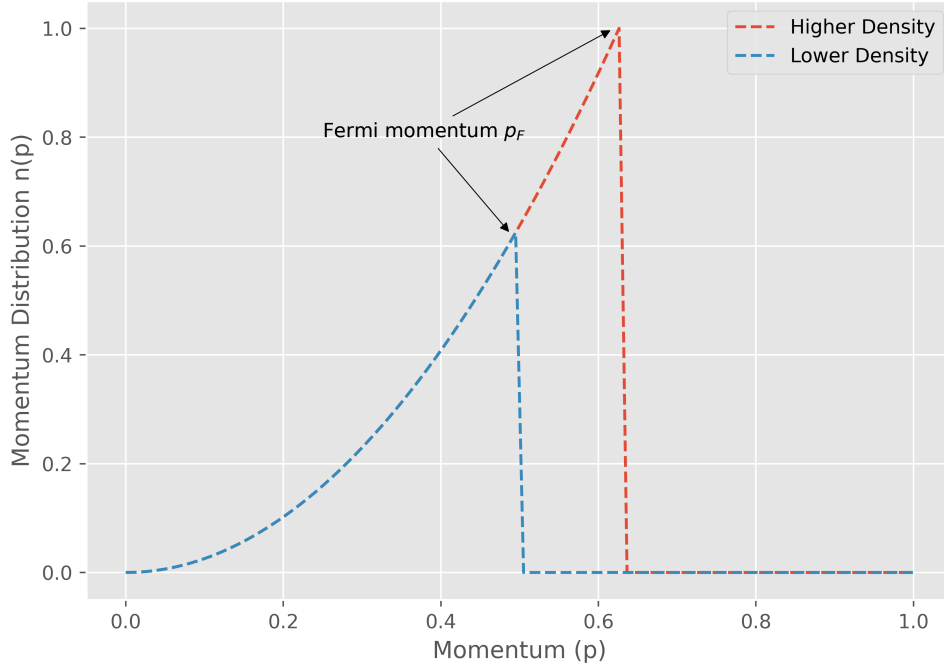


Fig. 2. Figure showing the momentum distribution of completely degenerate near-relativistic electrons modelled as a Fermi gas. The axis are in arbitrary units and the peak momentum p_F is labelled for 2 states of different densities.

nucleon Y_e , as $n_e = Y_e \rho / m_p$. The Fermi momentum can be represented as

$$p_F = h \left(\frac{3n_e}{8\pi} \right)^{1/3} = \left(\frac{3Y_e \hbar^3 \rho}{8\pi m_p} \right)^{1/3} = m_e c \left(\frac{\rho}{\rho_0} \right)^{1/3} \quad (15)$$

where

$$\rho_0 = m_p m_e^3 c^3 / 3\pi^2 \hbar^3 Y_e = 9.79 \times 10^8 Y_e^{-1} \text{ kg m}^{-3} \quad (16)$$

m_p is the mass of a proton (in kg), m_e is the mass of an electron (in kg), c is the speed of light (in m/s) and $\hbar = 1.05457148 \times 10^{-34} \text{ kg m}^2 \text{ s}^{-1}$, the reduced Planck constant.

The components needed to compute the pressure integral in Equation 6 have now been found. For the near-relativistic case the near-relativistic velocity from Equation 8 must be used, giving the pressure integral as

$$P = \frac{1}{3} \int_0^{p_F} p \sqrt{\frac{(p/m)^2}{1 + \frac{(p/m)^2}{c^2}}} \frac{8\pi p^2}{h^3} dp \quad (17)$$

where p is the momentum. Since the goal is $\frac{dP}{d\rho}$ the Newton-Leibniz integral rule can be used (Flanders 1973) which gives us the formula for the differentiation of a definite integral evaluated at the limit of the integral - effectively the integral can be "cancelled out". Using the chain rule:

$$\frac{dP}{d\rho} = \frac{dP}{dp} \frac{dp}{d\rho} \quad (18)$$

and then

$$\frac{dP}{d\rho} = \frac{8\pi}{3h^3} p_F^3 \sqrt{\frac{(p_F/m)^2}{1 + \frac{(p_F/m)^2}{c^2}}} \frac{dp}{d\rho} \Big|_{p_F} \quad (19)$$

If p_F from Equation 15 is subbed in, in terms of ρ and ρ_0 , then

$$\frac{dP}{d\rho} = \frac{8\pi m_e^3 c^3}{3h^3} \frac{\rho}{\rho_0} \sqrt{\frac{(\rho/\rho_0)^{2/3} c^2}{1 + \left(\frac{\rho}{\rho_0}\right)^{2/3}}} \frac{dp}{d\rho} \Big|_{p_F} \quad (20)$$

which simplifies to

$$\frac{dP}{d\rho} = \frac{8\pi m_e^3 c^4}{3h^3} \left(\frac{\rho}{\rho_0} \right)^{4/3} \frac{1}{\left(1 + \left(\frac{\rho}{\rho_0}\right)^{2/3}\right)^{1/2}} \frac{dp}{d\rho} \Big|_{p_F} \quad (21)$$

From Equation 15 the derivative of the momentum at p_F with respect to the density is

$$\frac{dp_F}{d\rho} = \frac{m_e c}{3\rho_0^{1/3} \rho^{2/3}} \quad (22)$$

which can be substituted in to give

$$\frac{dP}{d\rho} = \frac{8\pi m_e^4 c^5}{9h^3} \left(\frac{\rho}{\rho_0} \right)^{4/3} \frac{1}{\left(1 + \left(\frac{\rho}{\rho_0}\right)^{2/3}\right)^{1/2}} \frac{1}{\rho_0^{1/3} \rho^{2/3}} \quad (23)$$

Collecting factors of ρ and ρ_0

$$\frac{dP}{d\rho} = \frac{8\pi m_e^4 c^5}{9h^3 \rho_0} \frac{(\rho/\rho_0)^{2/3}}{\left(1 + \left(\frac{\rho}{\rho_0}\right)^{2/3}\right)^{1/2}} \quad (24)$$

Subbing in the definition for ρ_0 from Equation 16 some of the constants cancel, leaving

$$\frac{dP}{d\rho} = \frac{Y_e m_e c^2}{m_p} \frac{(\rho/\rho_0)^{2/3}}{3 \left(1 + \left(\frac{\rho}{\rho_0}\right)^{2/3}\right)^{1/2}} \quad (25)$$

This equation can be put into the form given below by taking out a factor of $\gamma(\rho/\rho_0)$

$$\frac{dP}{d\rho} = Y_e \frac{m_e c^2}{m_p} \gamma \left(\frac{\rho}{\rho_0} \right) \quad (26)$$

where γ is

$$\gamma(y) = \frac{y^{2/3}}{3(1 + y^{2/3})^{1/2}} \quad (27)$$

This is the form of the equation of state required to solve the differential equations and determine the structure of a white dwarf.

2.3. Dimensionless Equations

The next step toward numerically solving these equations is to make them dimensionless. This scales the variables to more reasonable numbers as inside white dwarfs there are very large pressures, densities and distances. If the variables were left most would be very large, but near the limits they could get much smaller, which could lead to rounding issues within the solving algorithm. The results of the solver can be reparametrized to be physically meaningful afterwards. To make these equations dimensionless define $x = \frac{r}{R_0}$, $y = \frac{\rho}{\rho_0}$ and $z = \frac{m}{M_0} = \frac{4\pi R_0^3 \rho_0}{3} \cdot x, y$ and z are dimensionless as they are defined as ratio between the variable and a constant of the same dimensions.

The equations of state can now be reparameterised in terms of these dimensionless variables. Firstly for Equation 5 m , r and ρ are replaced to get

$$\frac{dz}{dx} = 3x^2 y \quad (28)$$

Next Equation 4 is subbed in to get

$$\frac{d(\rho_0 y)}{d(R_0 x)} = - \left(\frac{dP}{d\rho} \right)^{-1} \frac{GM_0 z y \rho_0}{R_0^2 x^2} \quad (29)$$

After collecting terms and cancelling constants:

$$\frac{dx}{dy} = - \left(\frac{dP}{d\rho} \right)^{-1} \frac{GM_0 z y}{R_0 x^2} \quad (30)$$

Substituting for $\frac{dP}{d\rho}$, given in Equation 26 above, with the trivial substitution for $\gamma \left(\frac{\rho}{\rho_0} \right) = \gamma(y)$:

$$\frac{dy}{dx} = \frac{GM_0 m_p}{R_0 m_e c^2 Y_e} \frac{zy}{x^2 \gamma(y)} \quad (31)$$

By careful definition of R_0 via the constants in the above equation, the above differential equation can be made entirely dimensionless. Simply setting the constants equal to 1 and rearranging gives

$$\frac{GM_0 m_p}{R_0 m_e c^2 Y_e} = 1 \quad (32)$$

$$R_0 = \frac{GM_0 m_p}{m_e c^2 Y_e} \quad (33)$$

The next step is to substitute for the definitions of ρ_0 and M_0 given above to find

$$R_0 = \sqrt{\frac{9Y_e^2 \hbar^3 \pi}{4Gm_p^2 m_e^2 c}} \approx 1.336 \times 10^7 Y_e m \quad (34)$$

Using this definition for R_0 , Equation 31 reduces to

$$\frac{dy}{dx} = - \frac{zy}{x^2 \gamma(y)} \quad (35)$$

There are now 2 dimensionless differential equations to be solved numerically. The solutions can be transformed back into physical units by multiplying by the appropriate constant.

3. Method

3.1. Differential Equation Solver: Runge-Kutta 4(5)

To solve the system of differential equations consisting of Equation 28 and Equation 35, a Runge-Kutta 4(5) solver based on the equations from Dormand & Prince 1980 was used. In this solver the error is controlled to the fourth order, but the steps are computed to the 5th order. For a given step size h , the local error is $O(h^5)$, leading to global error of $O(h^4)$. The Runge-Kutta method solves a system of ordinary differential equations using the known starting value of the parameters (boundary conditions), and then computing further terms with a series of coefficients dependent on the step size. Very generally for a differential equation of form

$$\frac{dy}{dx} = f(x, y) \quad (36)$$

Runge-Kutta methods approximate y_{i+1} from the value of y_i . It is commonly used because only the starting value of y_i is needed, no differentiation is done and the function $f(x, y)$ is the only function used. However the method of computing the next value is somewhat complex, especially for higher-order methods, and multiple coefficients need to be computed before the value of y_i can be found (Riley et al. 2002). For the exact details of the equations and coefficients see Dormand & Prince 1980.

The Dormand-Price equations are an adaptive Runge-Kutta method, which vary the step size based on the difference between the 4th and 5th orders to keep it below a user-defined level. If the error is too high for a given step, it is repeated with a smaller size - if it is much smaller then to save time the step size is increased. There are lower order Runge-Kutta methods but RK4(5) provides a good balance between accuracy and computation time.

The RK45 method is implemented in Python using SciPy's `solve_ivp` and `RK45` (Virtanen et al. 2020). This allows an arbitrary interval of integration and independent setting of the points at which the solution is evaluated - i.e it can be solved at much higher precision than is actually returned by the solver.

The Runge-Kutta method integrates outward from the centre of the star, so the boundary conditions are that the enclosed mass (m) is 0, and the central density is a value ρ_c . The value of ρ_c is varied to model stars of different total masses. For an adaptive solver the error is controlled by two parameters - absolute (α_a) and relative (α_r) error. For each step the error is controlled to be below $\alpha_a + \alpha_r \times |y|$ where $|y|$ is the magnitude of the solution at that point. Here both are set to 10^{-7} to ensure high accuracy in the solution and to keep the global error low.

The solutions are computed for 10,000 x values between 10^{-7} and 20 which was determined to produce a smooth solution across the entire relevant range in density/mass space while

Star	M/M_{\odot}	R/R_{\odot}
Standard white dwarfs		
Sirius B	1.0034 ± 0.026	0.00840 ± 0.00025
G226-29	0.750 ± 0.030	0.01040 ± 0.0003
G93-48	0.750 ± 0.060	0.01410 ± 0.0020
CD -38 10980	0.740 ± 0.040	0.01245 ± 0.0004
L268-92	0.700 ± 0.120	0.01490 ± 0.0010
Stein 2051B	0.660 ± 0.040	0.0110 ± 0.0010
Procyon B	0.602 ± 0.015	0.01234 ± 0.00032
Wolf 485 A	0.590 ± 0.040	0.01500 ± 0.0010
L711-10	0.540 ± 0.040	0.01320 ± 0.0010
L481-60	0.530 ± 0.050	0.01200 ± 0.0040
40 Eri B	0.501 ± 0.011	0.01360 ± 0.0002
G154-B5B	0.460 ± 0.080	0.01300 ± 0.0020
Wolf 1346	0.440 ± 0.010	0.01342 ± 0.0006
Feige 22	0.410 ± 0.030	0.01367 ± 0.0020
Compact dwarfs		
GD 140	0.790 ± 0.020	0.00854 ± 0.0005
G156-64	0.590 ± 0.060	0.01100 ± 0.0010
EG 21	0.580 ± 0.050	0.01150 ± 0.0004
EG 50	0.500 ± 0.020	0.01040 ± 0.0006
G181-B5B	0.500 ± 0.050	0.01100 ± 0.0010
GD 279	0.440 ± 0.020	0.01290 ± 0.0008
WD2007-303	0.440 ± 0.050	0.01280 ± 0.0010
G238-44	0.420 ± 0.010	0.01200 ± 0.0010

Table 1. Table of white dwarf and compact dwarf masses, radii and associated uncertainties. Taken from Provencal et al. 1998.

keeping computation time to a reasonable level. A value just above 0 (10^{-9}) was used for the lower limit to prevent division by 0 errors. There is also a modification made to the $\frac{dz}{dx}$ to ensure it doesn't blow up for very small values of x by setting it to 0 for $x \leq 10^{-7}$. The ratio of central density ρ_c to ρ_0 varied for 1500 values spaced logarithmically between 10^{-2} and 10^9 which corresponds to a wide range of white dwarf masses, including up to the upper limit of white dwarf mass. The mass of the white dwarf is computed for each value of the central density by looking at the radius at which the density drops to a factor of 10^{-7} of the central value. The enclosed mass within this radius is then taken as the total mass of the white dwarf, and the radius as the outer radius of the white dwarf. A plot of mass against radius shows the mass-radius relation for each type of white dwarf.

The solutions are produced in terms of x , y and z , the dimensionless variables defined the derivation above, so to transform them back into physically meaningful values simply multiply by the relevant scaling constant. Because these constants, given in Equation 16 and 34, depend on Y_e , they will differ for stars of different constituent elements.

The results for the white dwarf mass-radius relations are compared to observed white dwarf masses and radii taken from online catalogs (via VizieR) accessed through Python using AstroQuery (Ginsburg et al. 2019).

4. Results and Discussion

Figure 3 shows a solution produced by the Runge-Kutta solver for the mass and density as a function of radius for a white dwarf of a particular central density ratio (1 in this case), corresponding to a white dwarf of total mass of $0.5 M_{\odot}$ for a C/O white dwarf, and $0.43 M_{\odot}$ for a Fe white dwarf. The density is much larger at smaller radii, and that there is a difference for C/O white dwarfs

and Fe white dwarfs. In general C/O white dwarfs have a larger radius for a given enclosed mass.

These curves were computed for 1500 different central densities and the total mass and radius was calculated for each, which is shown in Figure 4. Mass is presented on the x-axis as it is the defining variable for a star. The curves show the mass-radius relation for both Fe and C/O white dwarfs, along with dashed lines indicating the location of the Chandrasekhar mass for each type of white dwarf. The radii are given both in km and solar radii. 3 example white dwarfs, Sirius B, 40 Eri B and Stein 2051 are also shown and lie within error on one of the mass-radius curves. Their radii, masses and uncertainties are taken from Provencal et al. 1998. An uncertainty area is also shown on the plot for both mass-radius relations and the details of its derivation are given in Section 4.1. The results suggest that Sirius B is well modelled by a Carbon-Oxygen white dwarf. Other papers agree that Sirius B is likely to be a C/O white dwarf (Bond et al. 2017). The mass and of Stein 2051 measured by Hipparcos (Provencal et al. 1998) suggests it is a Fe white dwarf, but more recent observations have further constrained the mass to be $0.675 \pm 0.051 M_{\odot}$, which is shown in the figure (Sahu et al. 2017). This observation is highly accurate as it was done by gravitational lensing, and it puts Stein 2051 directly on the carbon-oxygen white dwarf line as expected. Inaccuracies in the Hipparcos white dwarf masses led to over predictions in the abundance of iron core white dwarfs.

The measurement of the mass and radius of 40 Eridani B from Provencal et al. (1998) has also been a subject of recent debate. As we can see from the plot, it suggests that 40 Eri B is well modelled by an iron white dwarf, which is inconsistent with theories of stellar evolution given the low mass of the white dwarf. In 2012 Giammichele et al. 2012 used a model atmosphere analysis to estimate the mass of 40 Eridani B by comparing the stellar spectra to obtain temp and gravity, and then constraining the mass using a theoretical mass-radius relationship. The authors found a mass of $0.59 M_{\odot}$, higher than found by Provencal et al. 1998. The disagreement of the 2 normally accurate methods was solved recently by Bond et al. 2017, who noticed the orbital parameters for 40 Eridani B were over 40 years old. They took new observations and found a smaller orbital period and hence a higher mass of $0.573 M_{\odot}$, which is within error of the result of Giammichele et al. 2012. This more accurate mass is plotted and is within error of the mass-radius relation for a carbon-oxygen white dwarf, as predicted for a star of this mass (Bédard et al. (2017)).

The line labelled as a C/O white dwarf also works in this model for any white dwarf consisting of elements with $Y_e = 0.5$. This includes He, ONe and ONeMg white dwarfs, of which all elements have one electron for every 2 nucleons. The differences come where on the curve the stellar population would fall, as the type of white dwarf formed depends on the progenitor star. Guo et al. 2021 suggests ONe or ONeMg white dwarfs below $\approx 1.1 M_{\odot}$ are not observed because the predecessor needs to be around $10 M_{\odot}$ to reach that stage of fusion burning, and models of stellar collapse suggest a star of that mass would not leave a core below $1.1 M_{\odot}$.

Figure 5 shows how the mass-radius relation in Figure 4 is constructed from the individual tracks (e.g Figure 3. The end point of each track corresponds to the outer radius and total mass of the white dwarf, and then the mass radius relation simply joins all these points into a continuous curve. It is shown for both C/O and Fe white dwarfs, and shows that while the individual tracks have similar qualitative shapes (as the same dimensionless equation is solved), the masses and radii reached are different.

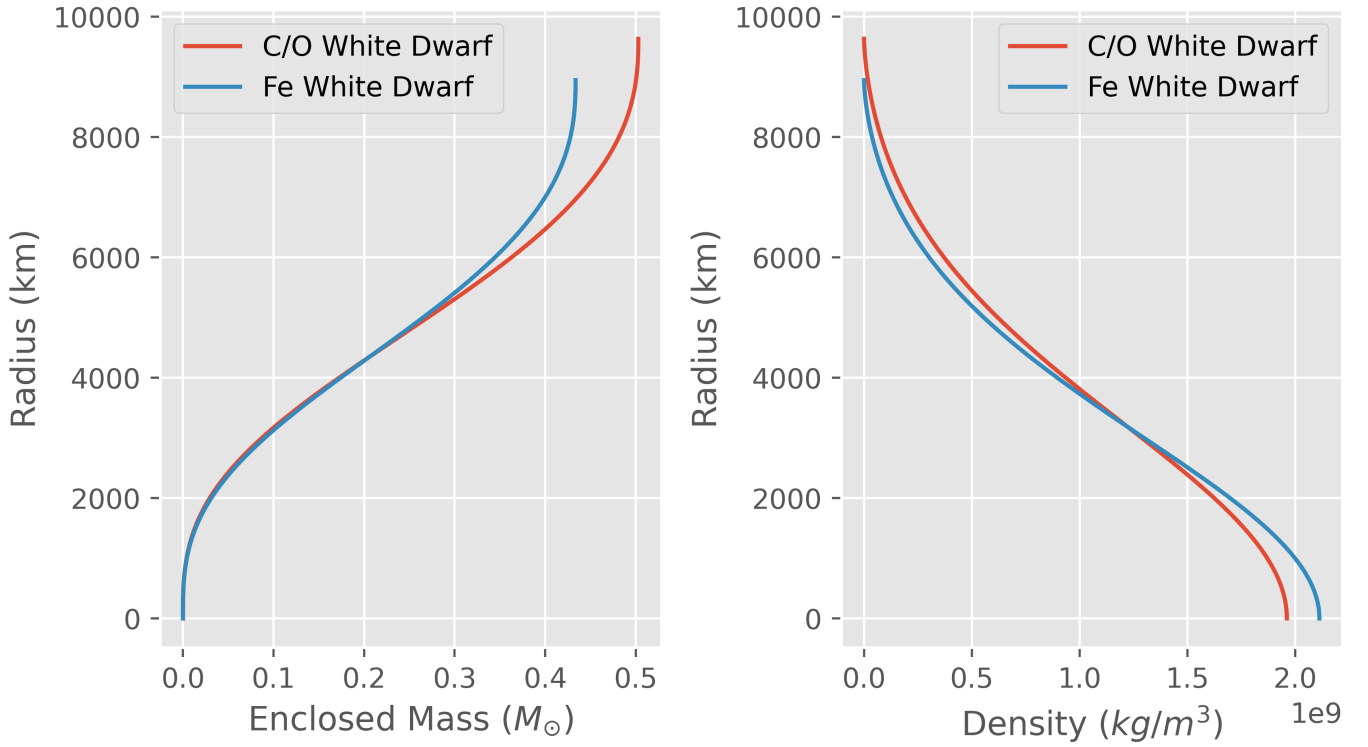


Fig. 3. Figure showing plots of radius against enclosed mass and density for typical C/O and Fe white dwarfs.

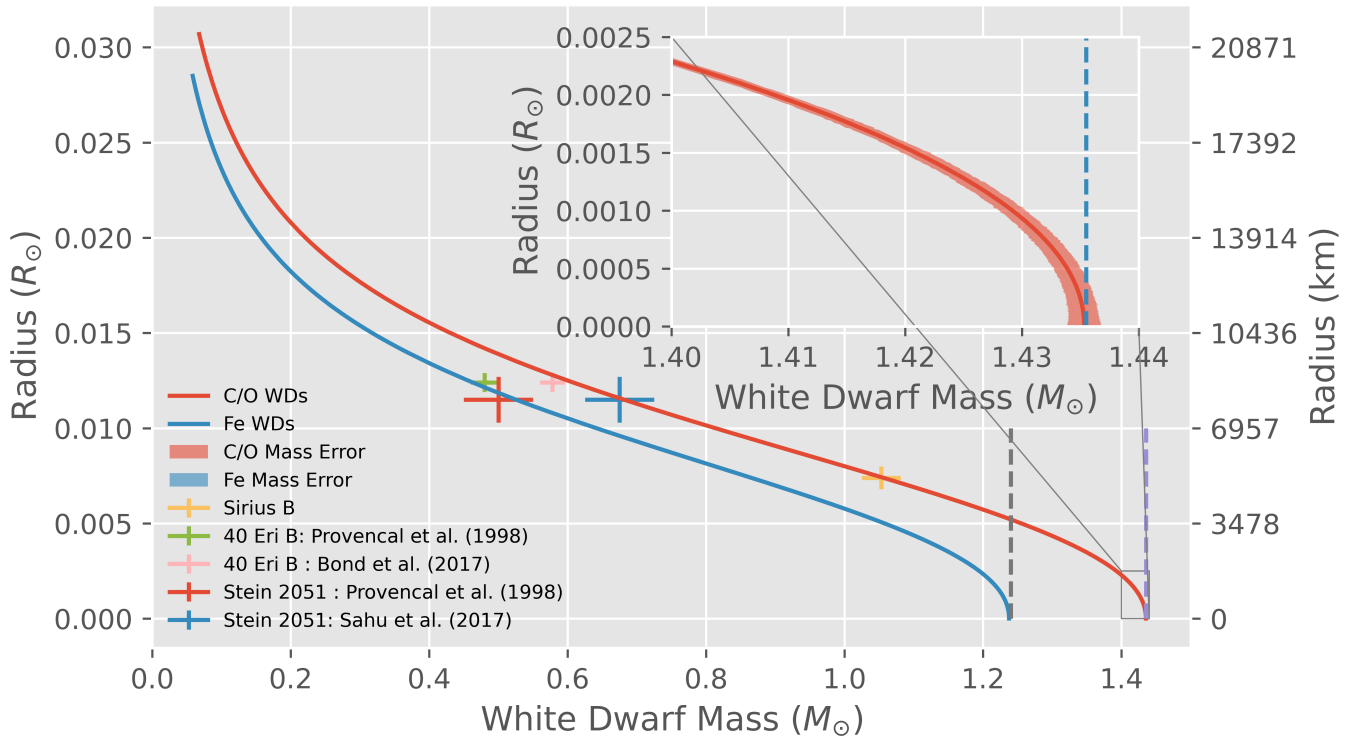


Fig. 4. Figure showing a plot of white dwarf radius as a function of mass for both C/O and Fe white dwarfs, along with the known masses and radii of several actual white dwarfs. Radii is shown both in km and solar radii, and the locations of the maximum (Chandrasekhar) mass is shown with a dotted line. The propagated uncertainties in the total mass at each point are shown by a lighter area around each line. The final section of the carbon-oxygen curve as it approaches the Chandrasekhar mass is shown in a subplot.

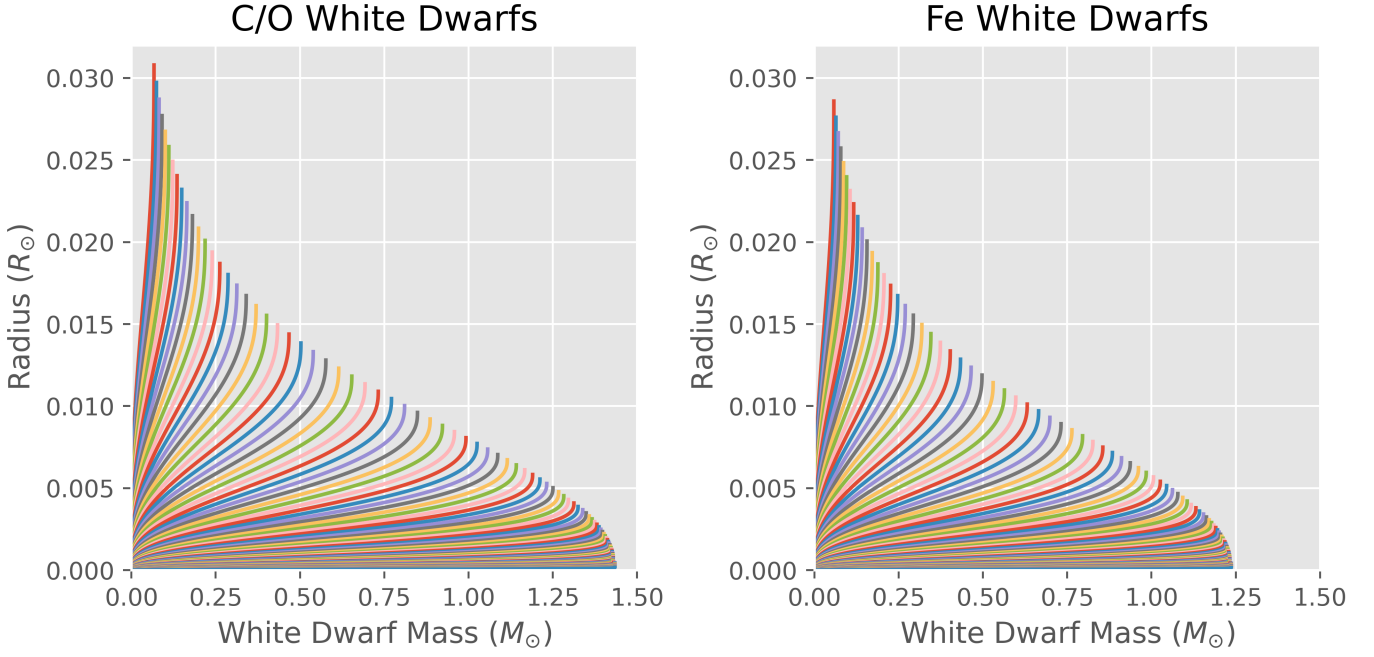


Fig. 5. Figure showing how the Radius-Mass plot for C/O and Fe white dwarfs in Figure 4 is produced from the individual curves for white dwarfs like Figure 3. Star mass (in solar masses) is plotted against radii (in stellar radii) for both Fe and C/O stars.

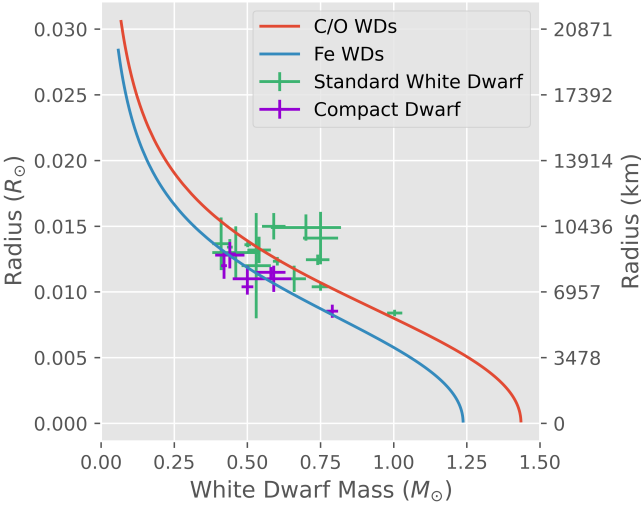


Fig. 6. Same figure as Figure 4 but with the masses, radii and associated uncertainties plotted for a greater variety of white dwarfs and compact dwarfs taken from Table 1.

Figure 6 shows the mass-radius curves plotted with the stars from Table 1 taken from Provencal et al. 1998. Plotted are both white dwarfs and compact dwarfs, many of which lie within error of either the carbon/oxygen or iron curves. Some of the points lie above the curve, reasons for which are addressed below. As addressed above, some of the stars shown here have since had better estimates of their mass that constrain them to be carbon-oxygen white dwarfs, and not Fe white dwarfs.

Figure 7 shows the mass-radius relations overlaid with a greater number of white dwarfs, which are derived from SDSS DR1 in Madej et al. 2019. They are for pure carbon white dwarfs with a hydrogen envelope, and are shown in red with associ-

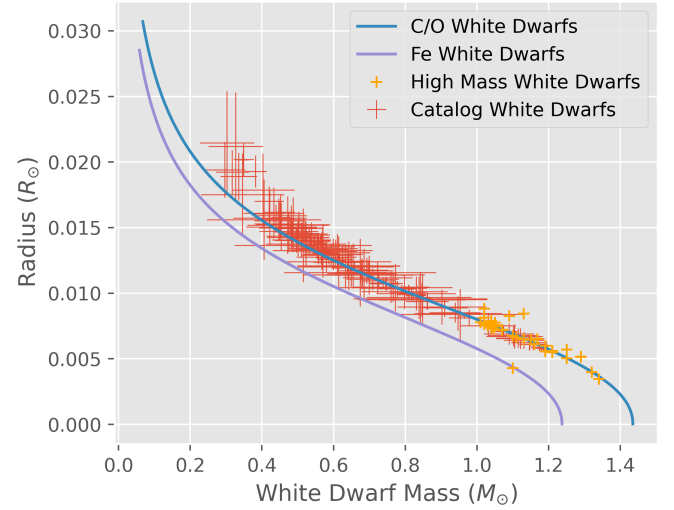


Fig. 7. Same figure as Figure 4 but with the masses, radii and associated uncertainties plotted for a selection of Carbon-Oxygen white dwarfs taken from the Madej et al. 2019 catalogue, accessed through Vizier.

ated mass and radii errors. High mass white dwarfs are shown in orange, taken from Należyty & Madej 2004 for white dwarfs greater than $1M_{\odot}$, and were not provided with errors. The SDSS DR1 white dwarfs follow the predicted trend increasingly well for higher stellar masses, with almost all of them being within error of the predicted curves. The high mass white dwarfs also appear very close to the predicted curve, but as errors were not provided it is not possible to say they are within error. The majority lie near the carbon-oxygen line, but there is one which lies on the Fe line at around $1.1M_{\odot}$.

4.1. Error Analysis

There are many complex ways to estimate the global error in the solution of a differential equation (for example Constantinescu 2015 and references therein) but in this case a simple upper estimate will be used. The source of error in this case is going to come from the simplicity of the model, and not from numerical deviations in the computations. The precision of the solution can be increased at very little computational cost to the point where the error bounds are negligible. A conservative upper limit of uncertainty in the ODE solution comes from

$$\alpha = N \times \Delta_{step} \quad (37)$$

where N is the number of steps the solver takes to solve the equations and Δ_{step} is the user-defined maximum variation in each step. Increasing the required precision does not increase the computing time considerably so it is easy to reduce the overall uncertainty in the solution to be negligible. The stars which have smaller mass and larger radius have a larger uncertainty in the mass because the solver takes more steps to solve them. The most massive stars have lower uncertainty because the solver completes with less steps while still achieving the same precision. This is demonstrated with an error curve for the mass-radius relation shown in Figure 4 which shows the variation in mass from errors propagated each Runge-Kutta solution. This was done with an absolute precision of 10^{-6} for demonstration purposes, as the actual value of 10^{-8} produced very small error bars. The error leads to a small error in the Chandrasekhar mass of $(1.44 \pm 0.002)M_{\odot}$ for carbon-oxygen white dwarfs, and $(1.24 \pm 0.001)M_{\odot}$ for Fe white dwarfs. These Chandrasekhar masses are within error of those derived in Chandrasekhar 1931 and given in Section 1.

This error analysis does not include the deviation of the assumptions of the model from the actual parameters of the star. The equation of state used is relatively simple and the stellar model doesn't take into account much of the physics that occurs. White dwarfs are incredibly complex objects that there is still much to learn about, and there are many subtleties unaccounted for here. In reality there are effects such as crystallisation (Tremblay et al. 2018) and rotation of white dwarfs that can change the equation of state and force balance inside the star.

5. Evaluation and Improvements

The assumptions in this model work well for the cores of white dwarfs, but the model assumes complete electron degeneracy even in the very outer lower density region of the star where the density would be low enough that the electrons would no longer be degenerate. In reality C/O and more exotic (ONeMg and Fe) white dwarfs are thought to have successive layers of outer degenerate envelopes (helium and then hydrogen) which contain some of the mass of the star. The thickness of these envelopes are thought to be proportional to g^{-1} where g is the surface gravity Camenzind 2007. This means lower mass white dwarfs have much thicker envelopes than higher mass white dwarfs. These envelopes often contain between 10^{-2} and 10^{-4} of the mass of the star (Romero et al. 2019). The combination of these factors is why the lower mass white dwarfs in Figure 7 diverge from the predicted curve. According to Romero et al. 2019 the outer hydrogen/helium envelope can increase the radius of the white dwarf by up to 20%. The model is closer to the observations for the higher mass white dwarfs with much smaller envelopes and more highly degenerate regimes where the assumptions are more accurate.

Many white dwarfs are also found in binary systems where they can be affected by a binary companion, e.g by roche-lobe accretion (Mohamed & Podsiadlowski 2007). This will affect the composition and thickness of the envelope and can lead to novae. As mentioned previously, the age of the white dwarf is also an important consideration, as the equation of state changes for older white dwarfs that begin to crystallise into a bcc lattice structure, starting from the core and moving outward (Tremblay et al. 2018). Rotation is another factor not considered in this paper that would be needed in a more general solution, as Anand 1965 found it can increase the Chandrasekhar mass of a C/O white dwarf to $1.704M_{\odot}$. Hermes et al. 2017 suggests almost all white dwarfs will be rotating as consequence of conservation of angular momentum, but the periods of rotation are long enough that the effect of the rotation is unlikely to be this high for the vast majority of white dwarfs.

Another improvement could come from using a more accurate equation of state that model the changing proportions of elements with radii and a proper electron distribution not and not a step function that accounts for the partially degenerate outer regions (crust) of the white dwarfs. It would be more accurate to use a proper modelling library like Modules for Experiments in Stellar Astrophysics (MESA) (Paxton et al. 2010). It considers the temperature, surface gravity and stellar atmosphere (hydrogen envelope, outer nuclear burning region etc) and often compare total luminosity to observations in order to calculate total surface area of the star (Koester 2010), and produces more physically realistic results.

The effects of general relativity on the mass-radius relations have not been accounted for, as instead of using the Newtonian equation of hydrostatic equilibrium, the Tolman-Oppenheimer-Volkoff (TOV) equation should be used instead (Tolman 1939, Oppenheimer & Volkoff 1939). This requires solving the metric of the interior of the star using Einstein's field equation considering the energy/momentum tensor of an ideal fluid. There are also further effects from Coulomb interactions and other small corrections that were accounted for in the Salpeter equations Salpeter 1961) which lead to deviations from ideal degeneracy assumed in this paper. Mathew & Nandy 2017 have shown the Salpeter and TOV modifications change the Chandrasekhar masses by more than 3%.

Overall the use of a simple Fermi degenerate near-relativistic electron gas has been shown to accurately model the interiors of white dwarfs and reproduce within error the mass-radius relation observed in stellar white-dwarf populations for carbon-oxygen white dwarfs. The model begins to break down for low-mass white dwarfs (below around $0.4M_{\odot}$ as the assumptions are no longer valid.

6. Conclusions

1. The equation of state of a white dwarf has been derived by modelling the star as a near-relativistic degenerate Fermi electron gas.
2. The differential equations relating the mass, density and radii of the white dwarf have been derived and manipulated into a dimensionless form suitable for computational analysis.
3. These equations and the equation have state have been solved simultaneously using SciPy's implementation of the Runge-Kutta 4(5) ODE solver to produce mass-radius and density-radius relations for a white dwarf of a given central density and composition.

4. The central density was varied between a factor 10^{-2} and 10^9 of a reference scale density in order to model white dwarfs of varying total mass.
5. The enclosed mass at a very low density was used to determine the total mass and radius of the white dwarf for each central density, and these were used to derive the overall mass-radius relation for white dwarfs.
6. The Chandrasekhar mass (upper mass limit) for both carbon-oxygen and iron white dwarfs were calculated from the mass-radius relations to be $(1.44 \pm 0.002)M_{\odot}$ and $(1.24 \pm 0.001)M_{\odot}$ respectively.
7. The mass-radius relations were compared to online catalogs of known white dwarf masses and radii, and where errors were available were mostly within error of the predicted relationship, especially for higher mass white dwarfs. It has been shown that Sirius B and Stein 2051, known white dwarfs, fall in the right place in the mass-radius relation to be carbon-oxygen white dwarfs, which is backed up by other papers.
8. There was some discrepancy between the predicted and observational data for lower mass white dwarfs which has been attributed to the simplicity of the model not accounting for deviations from degeneracy at high radii, and the lack of modelling of the outer hydrogen/helium envelopes that are observed in white dwarfs.
9. Overall the results from the model match observations, and the success of modelling the white dwarf simply has been demonstrated. Further improvements could include accounting for the effects of general relativity, hydrogen envelopes and deviations from electron degeneracy to increase the accuracy of the model.

Acknowledgements. This research has made use of NASA's Astrophysics Data System. This research has made use of the VizieR catalogue access tool, CDS, Strasbourg, France.

References

- Anand, S. 1965, Proceedings of the National Academy of Sciences of the United States of America, 54, 23
- Bédard, A., Bergeron, P., & Fontaine, G. 2017, The Astrophysical Journal, 848, 11
- Benvenuto, O. G. & De Vito, M. A. 2005, Monthly Notices of the Royal Astronomical Society, 362, 891
- Bond, H. E., Bergeron, P., & Bédard, A. 2017, The Astrophysical Journal, 848, 16
- Bond, H. E., Schaefer, G. H., Gilliland, R. L., et al. 2017, ApJ, 840, 70
- Camenzind, M. 2007, Compact objects in astrophysics (Springer)
- Catalán, S., Ribas, I., Isern, J., & García-Berro, E. 2007
- Chandrasekhar, S. 1931, ApJ, 74, 81
- Constantinescu, E. 2015, arXiv preprint arXiv:1503.05166
- Dirac, P. A. M. 1926, Proceedings of the Royal Society of London. Series A, Containing Papers of a Mathematical and Physical Character, 112, 661
- Dormand, J. R. & Prince, P. J. 1980, Journal of computational and applied mathematics, 6, 19
- Eisenstein, D. J., Liebert, J., Harris, H. C., et al. 2006, ApJS, 167, 40
- Flanders, H. 1973, The American Mathematical Monthly, 80, 615
- Fowler, R. H. 1926, Monthly Notices of the Royal Astronomical Society, 87, 114
- Gentile Fusillo, N. P., Tremblay, P.-E., Gänsicke, B. T., et al. 2018, Monthly Notices of the Royal Astronomical Society, 482, 4570–4591
- Giammichele, N., Bergeron, P., & Dufour, P. 2012, ApJS, 199, 29
- Ginsburg, A., Sipőcz, B. M., Brasseur, C. E., et al. 2019, The Astronomical Journal, 157, 98
- Guo, Y., Liu, D., Wu, C., & Wang, B. 2021, Research in Astronomy and Astrophysics, 21, 034
- Hambly, N. C., Smartt, S. J., & Hodgkin, S. T. 1997, ApJ, 489, L157
- Heisenberg, W. 1927, Zeitschrift für Physik, 43, 172
- Hermes, J., Gänsicke, B., Kawaler, S. D., et al. 2017, The Astrophysical Journal Supplement Series, 232, 23
- Herschel, W. 1785, Philosophical transactions of the Royal Society of London, 40
- Hillebrandt, W. & Niemeyer, J. C. 2000, ARA&A, 38, 191
- Isern, J., Canal, R., & Labay, J. 1991, The Astrophysical Journal, 372, L83
- Kepler, S. O., Kleinman, S. J., Nitta, A., et al. 2007, Monthly Notices of the Royal Astronomical Society, 375, 1315
- Kleinman, S. J., Kepler, S. O., Koester, D., et al. 2013, ApJS, 204, 5
- Koester, D. 2010, Memorie della Società Astronomica Italiana, 81, 921
- Liebert, J., Bergeron, P., Eisenstein, D. J., et al. 2004, Astrophys. J., 606, L147
- Madej, J., Nalezyty, M., & Althaus, L. G. 2019, VizieR Online Data Catalog, J/A+A/419/L5
- Marshak, R. E. 1940, The Astrophysical Journal, 92, 321
- Mathew, A. & Nandy, M. K. 2017, Research in Astronomy and Astrophysics, 17, 061
- McCook, G. P. & Sion, E. M. 1999, The Astrophysical Journal Supplement Series, 121, 1
- Mohamed, S. & Podsiadlowski, P. 2007, in 15th European Workshop on White Dwarfs, Vol. 372, 397
- Nalezyty, M. & Madej, J. 2004, Astronomy & Astrophysics, 420, 507
- Nomoto, K. 1984, ApJ, 277, 791
- Oberhammer, H., Csótó, A., & Schlattl, H. 2000, Science, 289, 88
- Oppenheimer, J. R. & Volkoff, G. M. 1939, Physical Review, 55, 374
- Paxton, B., Bildsten, L., Dotter, A., et al. 2010, The Astrophysical Journal Supplement Series, 192, 3
- Pols, O. 2011, STELLAR STRUCTURE AND EVOLUTION (Astronomical Institute Utrecht)
- Provencal, J. L., Shipman, H. L., Hog, E., & Thejll, P. 1998, The Astrophysical Journal, 494, 759
- Riley, K. F., Hobson, M. P., Bence, S. J., & Hobson, M. 2002, Mathematical methods for physics and engineering: a comprehensive guide (Cambridge university press)
- Romero, A. D., Kepler, S. O., Joyce, S. R., Lauffer, G., & Córscico, A. H. 2019, Monthly Notices of the Royal Astronomical Society, 484, 2711
- Sahu, K. C., Anderson, J., Casertano, S., et al. 2017, Science, 356, 1046
- Salpeter, E. E. 1961, The Astrophysical Journal, 134, 669
- Sarna, M., Ergma, E., & Gerškevič, J. 2001, Astronomische Nachrichten, 322, 405
- Shipman, H. L. 1979, ApJ, 228, 240
- Tolman, R. C. 1939, Physical Review, 55, 364
- Tremblay, P.-E., Fontaine, G., Fusillo, N. P. G., et al. 2018, University of Warwick
- Tremblay, P. E., Gentile-Fusillo, N., Raddi, R., et al. 2017, MNRAS, 465, 2849
- Virtanen, P., Gommers, R., Oliphant, T. E., et al. 2020, Nature Methods, 17, 261
- Woosley, S. E., Heger, A., & Weaver, T. A. 2002, Reviews of Modern Physics, 74, 1015
- Xu, S., Lai, S., & Denrihy, E. 2020, ApJ, 902, 127